Experimental Modification and Identification of the DSS-13 Antenna Control System Model

C. S. Racho and W. K. Gawronski
Ground Antennas and Facilities Engineering Section

This work is the first step toward increasing the bandwidth of the DSS-13 antenna position loop controller. A wider bandwidth of the controller allows for faster tracking rates and better pointing performance under windy conditions. To achieve this goal, the antenna control system model has to be improved, such that it will accurately reflect the dynamic properties of the antenna. The existing analytical model, due to its many uncertainties, could not be used in the design of the controller. However, by using experimental data, the analytical model is modified and improved, and a new model is obtained through system identification techniques.

I. Introduction

The position controller at the DSS-13 beam-waveguide antenna does not employ model-based control law. In the interest of implementing model-based control law at the DSS-13 antenna, an analytical model of this antenna was developed [1]. The experiment described in this article was then designed to validate this analytical model and to identify a new antenna model from the experimental data (the latter model will be referred to as the experimental model). The data collected by this experiment at the DSS-13 antenna were collected for each axis separately. The data were processed and used to modify the analytical model and to obtain an experimental model through system identification techniques. Since the latter approach requires only a portion of the data, a sample was taken from the remaining data and used to validate the experimental model.

II. Description of the Experimental Software and Hardware

The purpose of this experiment is to gather time series data on the input to the antenna drives and the output of the antenna position. These data are processed to determine the frequency responses, or transfer functions, of the DSS-13 antenna. These transfer functions represent an open-loop system. They are used as a reference to determine the correction of the parameters of the analytical model, and also to identify the transfer function of the system using identification software.

A. Experimental Software

The LabView 2 application software generates an analog random (white noise) signal. This signal is input into the rate loop via the test input lead in the servo interface chassis, and the encoder output is sampled from the data converter. The input and the output signals are buffered until the designated number of samples is taken. The sampled data are then saved in floating point MATLAB[1] loadable format files.

B. Experimental Hardware

The data acquisition system consists of the LabView 2 software running on a Macintosh IIfx computer. The com-

---

[1] Copyright 1985–91, Inc. All rights reserved.

puter contains an analog board which can output analog signals through two channels to the antenna rate loop. It also contains two digital boards which sample the azimuth and the elevation position encoder output (Fig. 1).

The National Instrument NB-MIO-16 multifunction analog board for the Macintosh is used to produce the analog rate signals injected into the antenna rate loop. The board contains two 12-bit digital-to-analog converters with voltage outputs. These two analog outputs are hooked up to the test input leads of either the azimuth or the elevation rate input, or both. The test inputs are located in the servo's interface chassis. The servo interface is switched to manual mode so that a rate signal is accepted from the test input lead instead of the antenna position controller. The brakes in both axes are released manually before the experiment begins.

The National Instrument's NB-DIO-32F 32-bit, parallel, digital, input/output interface board for the Macintosh II is used to sample the binary output of the data converter. The data converter buffers the 24 bits of encoder data available in each axis and provides the data in latched binary form.

A Hewlett Packard frequency counter is used to measure the sample period for each run of the experiment, since the sample period depends on the execution speed of the LabView 2 software, and it cannot be determined in advance.

C. Data Acquisition

The experimental data were collected separately for each axis, namely, for elevation rate input to elevation position output, elevation rate input to azimuth position output, azimuth rate input to azimuth position output, and azimuth rate input to elevation position output. The maximum rate analog input voltage was 1.3 V, and the minimum was 0.1 V.

For each axis and each of its cross couplings, the experimental data were taken in separate sequences. Each sequence contained 8192 data points, and there were anywhere between 10 and 40 sequences per run of the experiment per axis. The available travel in the elevation axis, in conjunction with the rate input and the sample interval, restricted the number of sequences that could be taken per run of the experiment. The azimuth axis, with 450 deg of travel from one limit to the other, never proved to be a limiting factor given the same rate input and sample period.

The data were gathered on several occasions. On each occasion, the wind speeds at DSS 13 were low (between 0

and 3.6 m/sec). When no input was applied to the elevation axis, data were taken for the elevation fixed at both 90 and 60 deg. When no input was applied to the azimuth axis, it was left fixed at 140 deg.

III. Analysis

A model-based control is currently not employed at the DSS-13 antenna. In order to design a model-based controller, a suitably accurate antenna model is required. There were two approaches taken to obtain such a model. First, the model presented in [1] was adjusted to fit the data collected in this experiment. In a second approach, a model was obtained by using a system identification technique based on the data.

A. Model Description

There are two analytical models for the DSS-13 antenna [1,2]: a model for the antenna at 90 deg elevation, and the other for the antenna at 60 deg elevation. These models are described in the state space form

$$\dot{x} = Ax + Bu, \qquad y = Cx \qquad (1)$$

In this model, the state vector x is of dimension n, the input u is of dimension p, the output y is of dimension q, and the matrices A, B, and C are of dimensions $n \times n$, $n \times p$, and $q \times n$, respectively. The full order of the analytical model in [1] is $n = 90$, and the reduced order model is $n = 27$. For the system whose input is azimuth and elevation rate and whose output is azimuth and elevation position, $p = 2$ and $q = 2$, and

$$B = [B_{az} B_{el}], \qquad C = \begin{bmatrix} C_{az} \\ C_{el} \end{bmatrix} \qquad (2)$$

where B_{az} and B_{el} represent azimuth and elevation input rate, and C_{az} and C_{el} represent azimuth and elevation encoder position.

The four transfer functions (elevation rate to elevation encoder position, elevation rate to azimuth encoder position, azimuth rate to azimuth encoder position, and azimuth rate to elevation encoder position) are used to compare analytical and experimental data. Let $T_{ij}(s)$ be the transfer function defined by

$$T_{ij}(s) = C_i(sI - A)^{-1}B_j, \qquad i,j = az, el \qquad (3)$$

By judiciously varying a set of A, B_i, and C_j matrices, one changes the transfer functions such that they better fit the empirical transfer functions. A "good" fit is required only over the frequency range where high coherence between input and output is observed, in most cases for frequencies from 0.01 to 10 Hz. In this case, the good fit means that the peak frequencies and magnitudes of the model transfer function line up with those of the empirical transfer function.

B. Frequency Responses of the DSS-13 Antenna

Using frequency domain analysis, the data were used to modify the analytical model. The input, $u(t)$, and output, $y(t)$, time series data have been detrended and passed through a Hanning filter to prevent spectral leakage [3]. Then, a fast Fourier transform (FFT) was performed on the resulting time series data. The magnitude of the transfer function, $T_{uy}(f)$, and the coherence, $\gamma_{uy}(f)$, were estimated from the time series data (c.f., [3]) using $u(t)$ and $y(t)$, filtered and detrended input and output vectors of 8192 samples each.

$$T_{uy}(f) = \frac{P_{uy}(f)}{P_{uu}(f)} \qquad (4)$$

$$\gamma_{uy} = \frac{|P_{uy}(f)|^2}{P_{uu}(f)P_{yy}(f)} \qquad (5)$$

where $P_{uu}(f)$ is the power spectral density estimate of $u(t)$, $P_{yy}(f)$ is the power spectral density estimate of $y(t)$, and $P_{uy}(f)$ is the cross spectral density estimate of $u(t)$ and $y(t)$. The phase is estimated from the time series data by using the following formula:

$$\phi(f) = \arctan\frac{Im(T_{uy})}{Re(T_{uy})} \qquad (6)$$

where $Re(.)$ and $Im(.)$ denote real and imaginary parts.

The transfer function estimates were obtained by averaging the magnitude and phase of each sequence. The magnitude, $T_{uy}(f)$, and the phase, $\phi_{uy}(f)$, are plotted versus frequency in Figs. 2(a)–(f) (dashed line), where $f = \omega/2\pi$ is frequency in Hz, and ω is frequency in rad/sec. In Figs. 3(c), 4(c), 5(c), and 6(c), the coherence was also plotted to determine the range of frequencies over which the data were valid.

C. Modification of the Analytical Model

The analytical model as described in [1] is a combination of the antenna structural model and models of the elevation and azimuth drives. It is derived from the best available knowledge of the antenna structure and servos. The antenna structural model is obtained from its finite element model. Although complex, as the finite element model usually is, its accuracy is still limited. For example, damping ratios or "non-structural" masses, such as counterweight mass, are usually only roughly estimated. The available field data allow one, to some extent, to correct some parameters of the analytical model so that its properties fit more closely the properties derived from the experiments. In addition, the drive models have some uncertainties. The gearbox stiffness is not known precisely, since it depends on the countertorque value, which is itself a fuzzy number. Also, the gains of the drive amplifiers are not set precisely, or can change. These and other less known factors impact the model accuracy.

D. System Identification Model

A second model is identified directly from the experimental data using the system identification software System/Observer/Controller Identification Toolbox (SOCIT), written in the MATLAB language [4]. The "okid" function of SOCIT identifies a state space model, i.e., the A, B, and C matrices, given the input–output data, sample period, and the number of observer Markov parameters. For more detailed information about SOCIT software and this function, the reader is referred to [4] and [5].

The SOCIT software was used to identify a model for each axis and cross-axis, so that the A, B, and C state space matrices were obtained for each subsystem. The order of the system was chosen based on the system's Hankel singular values plotted as part of the okid function output. Typically, the order chosen was between 25 and 30. The resulting state space matrices were transformed into balanced coordinates, so that a matrix A was in diagonally dominant form. The 2 × 2 diagonal blocks represent the system modes in decreasing order of importance. The diagonal elements of a 2 × 2 block represent the system damping, and the off-diagonal elements represent natural frequencies at those modes.

The order of each subsystem was reduced to the smallest acceptable order, i.e., such that all the modes visible in the data up to 10 Hz were preserved. The order, n, of the T_{azaz}, T_{azel}, T_{elel}, and T_{elaz} subsystems was $n = 14$, 13, 10, and 11, respectively. The identified model had some discrepancies (with respect to the experimental data) which apparently could be removed. Namely, the damping

ratios were adjusted for the system modes which appear either underdamped or, more commonly, overdamped.

These four identified subsystems are then used to simulate time series responses, given the actual input data, u_{az} or u_{el}, and small bias signals, u_{azb} or u_{elb},

$$y_{azaz}^s = T_{azaz}u_{az} \qquad (7a)$$

$$y_{azel}^s = T_{azel}u_{az} + T_{elel}u_{elb} \qquad (7b)$$

$$y_{elel}^s = T_{elel}u_{el} \qquad (7c)$$

$$y_{elaz}^s = T_{azaz}u_{azb} + T_{elaz}u_{el} \qquad (7d)$$

The use of small bias in the cross-coupling responses was necessary because the straight gains $| T_{azaz} |$ and $| T_{elel} |$ are much larger than the cross gains $| T_{azel} |$ and $| T_{elaz} |$. For the same reason, the bias can be neglected in the straight responses (azimuth-to-azimuth and elevation-to-elevation). The simulated responses, y_{azaz}^s, y_{azel}^s, y_{elel}^s, and y_{elaz}^s, were compared to the actual SISO output data, y_{azaz}, y_{azel}, y_{elel}, and y_{elaz}, and the approximation errors in azimuth and elevation, ϵ_{azaz}, ϵ_{azel}, ϵ_{elel}, and ϵ_{elaz}, were computed.

$$\epsilon_{azaz} = \frac{\| y_{azaz} - y_{azaz}^s \|}{\| y_{azaz} \|} \times 100\% \qquad (8a)$$

$$\epsilon_{azel} = \frac{\| y_{azel} - y_{azel}^s \|}{\| y_{azel} \|} \times 100\% \qquad (8b)$$

$$\epsilon_{elel} = \frac{\| y_{elel} - y_{elel}^s \|}{\| y_{elel} \|} \times 100\% \qquad (8c)$$

$$\epsilon_{elaz} = \frac{\| y_{elaz} - y_{elaz}^s \|}{\| y_{elaz} \|} \times 100\% \qquad (8d)$$

These formulas estimate the relative discrepancy between the measured and simulated signals.

IV. Discussion of the Results

A. Results of Analytical Model Adjustments

The magnitude plots of the four transfer functions obtained from the analytical model (solid line) and from the experimental data (dashed line) are shown in Figs. 7(a)–(d). The discrepancies between the analytical and experimental transfer functions are immediately obvious. In particular, there is a mismatch in the first resonance frequency in the azimuth-to-azimuth and elevation-to-elevation transfer functions, and there are higher resonance peaks in the analytical model for almost all resonance frequencies. The mismatch in the first fundamental frequencies is due to the underestimation of nonstructural masses in the structural analysis. The high peaks at the resonance frequencies are caused by an assumption of very low structural damping (0.5 percent). Modifying the rigid-body structural masses (an increase of 45 percent in the elevation rigid body modal mass and an increase of 70 percent in the azimuth rigid-body modal mass) and increasing modal damping for the higher frequency modes to 5 percent improves the fit between the analytical model and experimental transfer function curves. Further improvement is obtained by adjusting the drive parameters. In the elevation and azimuth drives, the amplifier gain, denoted k_r in [1], is reduced by 30 percent (from 80 to 56), and in the azimuth drive, the gear box stiffness is reduced by 15 percent (from 2×10^7 to 1.7×10^7). The results of the modifications of the analytical model show a better fit to the experimental results, as seen in the solid-line plots of Figs. 2(a)–(d). The worst fit between the experimental and model transfer function curves occurs in the elevation input to azimuth output. This is due to the very small value of this function. It is at least 100 times smaller, in magnitude, than the elevation-to-elevation transfer function, or at least 10 times smaller than the azimuth-to-elevation transfer function. The complexity of the analytical model made it difficult to determine what other parameters were responsible for the remaining differences.

The significant modal frequencies as estimated from the data are shown in Table 1.

B. Results of System Identification

In Figs. 3, 4, 5, and 6, the identified transfer function plots are presented with the empirical transfer function plots. Both plots show low frequency anomalies. The cross-coupling transfer functions T_{elaz} and T_{azel} are expected to approach zero value at zero frequency, since no static coupling between elevation and azimuth or between azimuth and elevation is observed. However, in Figs. 4(a) and 5(a), such a tendency is not present. The magnitude of the transfer function from azimuth to azimuth or from elevation to elevation should roll off at a 20-dB/dec rate for low frequencies, since the system contains two integrators (or two poles at zero). This can be observed in the measured frequency range of these plots. However, for fre-

quencies lower than measured ($f < 0.01$ Hz), the identified transfer function does not rise.

The departure of the empirical transfer function plots from the expected zero value in the low frequencies is caused by the presence of a small bias at the input port where no signal is applied. For example, when an elevation rate signal is applied and the azimuth position is sampled, a small azimuth rate input still exists, and it shows up in the output data at low frequencies. Its presence is explained with the comparatively high gain for straight connection (azimuth-to-azimuth or elevation-to-elevation) when compared with the cross-connection (elevation-to-azimuth or azimuth-to-elevation). The unmeasured bias can be explained by the lack of causality between input and output in cross-coupling for low frequencies, as visible in the coherence plots of Figs. 4(c) and 5(c), where the coherence is almost zero. In order to correct this problem, the data were filtered with a high-pass filter before being used in the system identification software. As a result, the cross-coupling transfer function plots are obtained as seen in Figs. 4(b) and 5(b).

For the straight transfer functions (azimuth-to-azimuth or elevation-to-elevation), the discrepancies between the identified model and the empirical transfer function in the very low frequency range are due to the presence of two very small eigenvalues of the identified A. By setting them to zero, the discrepancies were eliminated.

The measurements were used to obtain both the adjusted model and the identified model. However, the identification software requires a relatively small portion of the data gathered. Hence, the remaining time series data, y_{azaz}, y_{azel}, y_{elel}, and y_{elaz}, taken at the DSS-13 antenna are compared to the simulated time series data, y^s_{azaz}, y^s_{azel}, y^s_{elel}, and y^s_{elaz}, of the identified model (Figs. 8–11). The discrepancy between the two signals, relative to the scale of the original signal, are computed using Eqs. (8a)–(8d).

An additional comparison was performed as follows. Define a positive function $r_i(k)$

$$r_i(k)\frac{\parallel y_i^m - k_i y_i^s \parallel}{\parallel y_i^m \parallel}, \quad i = el, \ az \qquad (9)$$

where superscripts m and s denote measured and simulated output, respectively. For $k_i = 1$, r_i shows the distance (or an approximation error) between the experimental and simulated data. One can further improve the fit between the experimental and simulated results by varying the parameter k_i. This additional fit is possible because the system was identified from a detrended set of data, but is compared to a non-detrended one. Let $r_i(k_i)$ achieve the minimal value for $k_i = k_{io}$, i.e., let $r_i(k_i) \geq r(k_{io})$. If $k_{io} = 1$, the simulated series is the best-fitted one and no modification is necessary. Thus, the gain adjustment factor δ_i, defined as

$$\delta_i =\mid k_{io} - 1 \mid \times 100\%, \qquad i = az, el \qquad (10)$$

is the measure of good fit. The gain factor δ_i is the percentage that the system gain is adjusted to improve the fit of the simulated time series y_{azaz} and y_{elel} to the measured time series y_{azaz} and y_{elel}.

The approximation errors and the gain factors are presented in Tables 2–5. Notice that the errors and factors are relatively close within each run of the experiment. The percentages for each run are of the same order and are small.

V. Conclusions

This article presents the use of experimental data collected at the DSS-13 beam waveguide antenna to adjust an existing analytical model and to identify a set of single-input, single-output models. Four models (azimuth-to-azimuth, azimuth- to-elevation, elevation-to-elevation, and elevation-to-azimuth) were obtained from the experiment. The measurement and analytical techniques used to arrive at both of these models are described. The experiment designed to gather the field data is also described in detail.

The next step is to obtain a viable and reasonably compact model of the DSS-13 antenna control system. The reduced-order models of the azimuth and elevation axes can and will be developed separately. Both models will then be used in the design of a model-based antenna position loop controller.

Acknowledgments

References

[1] W. Gawronski and J. A. Mellstrom, "Modeling and Simulations of the DSS-13 Antenna Control System," *The Telecommunications and Data Acquisition Progress Report 42-106, vol. April–June 1991,* Jet Propulsion Laboratory, Pasadena, California, pp. 205–248, August 15, 1991.

[2] W. Gawronski and J. A. Mellstrom, "Control and Dynamics of the Deep Space Network Antennas," *Control and Dynamic System,* vol. 57, edited by C. T. Leondes, San Diego, California: Academic Press, 1993.

[3] J. S. Bendat and A. G. Piersol, *Random Data, Analysis and Measurement Procedure,* 2nd ed., New York: Wiley, 1986.

[4] J.-N. Juang, L. G. Horta, and M. Phan, "System/Observer/Controller Identification Toolbox (SOCIT)," NASA Technical Memorandum 107566, Langley Research Center, Hampton, Virginia, February 1992.

[5] J.-N. Juang, M. Phan, L. G. Horta, and R. W. Longman, "Identification of Observer and Kalman Filter Markov Parameters: Theory and Experiment," *Proc. of the AIAA Guidance, Navigation, and Control Conf.,* New Orleans, Louisiana, pp. 1172–1179, August 1991.

Table 1. Natural frequencies, f Hz, of the four transfer functions.

f_{azaz}	f_{azel}	f_{elel}	f_{elaz}
1.65	1.62	2.01	1.98
3.24	3.26	3.15	3.21
4.24	4.21	5.22	5.30
–	5.76	–	–

Table 2. Approximation errors for the azimuth-to-azimuth time series.

Data set	ϵ_{azaz}, percent	δ_{az}, percent
1	0.31	0.69
2	0.21	1.00
3	0.27	1.01
4	0.27	1.32

Table 3. Approximation errors for the elevation-to-elevation time series.

Data set	ϵ_{elel}, percent	δ_{el}, percent
1	0.17	1.07
2	0.17	1.22
3	0.23	2.18
4	0.17	2.05

Table 4. Approximation errors for the azimuth-to-elevation time series.

Data set	ϵ_{azel}, percent	u_{elb}, V
1	6.81	0.0014
2	6.75	0.0013
3	6.36	0.0014
4	5.95	0.0014

Table 5. Approximation errors for the elevation-to-azimuth time series.

Data set	ϵ_{elaz}, percent	u_{azb}, V
1	4.12	0.0014
2	4.57	0.0014
3	4.66	0.0015
4	4.19	0.0014

Fig. 1. The experimental setup at the DSS-13 beam waveguide antenna.
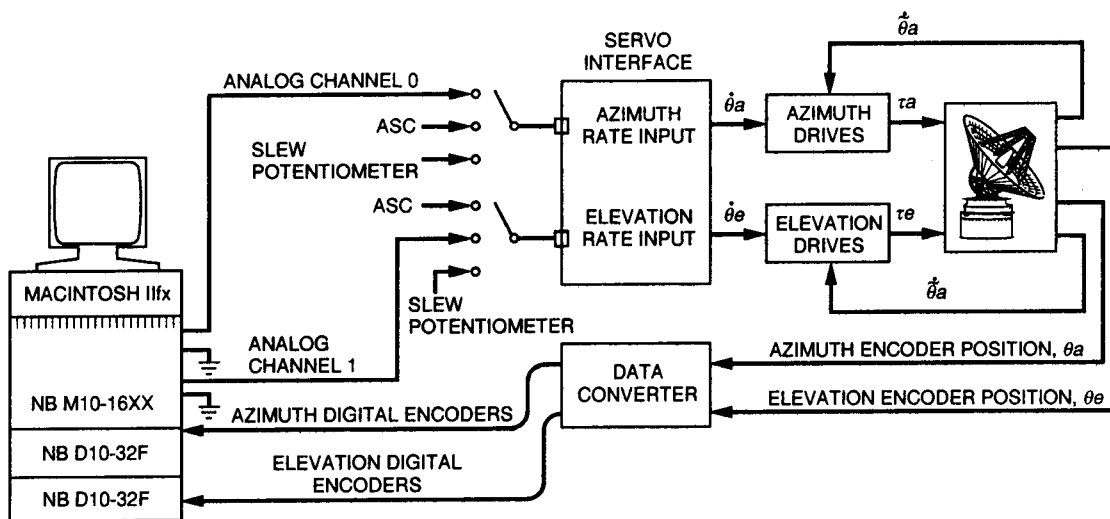
ASC = ANTENNA SERVO

$\dot{\theta}a$ = AZIMUTH RATE INPUT

$\dot{\theta}e$ = ELEVATION RATE INPUT

$\overset{*}{\dot{\theta}}a$ = AZIMUTH TACHOMETER FEEDBACK

$\overset{*}{\dot{\theta}}e$ = ELEVATION TACHOMETER FEEDBACK
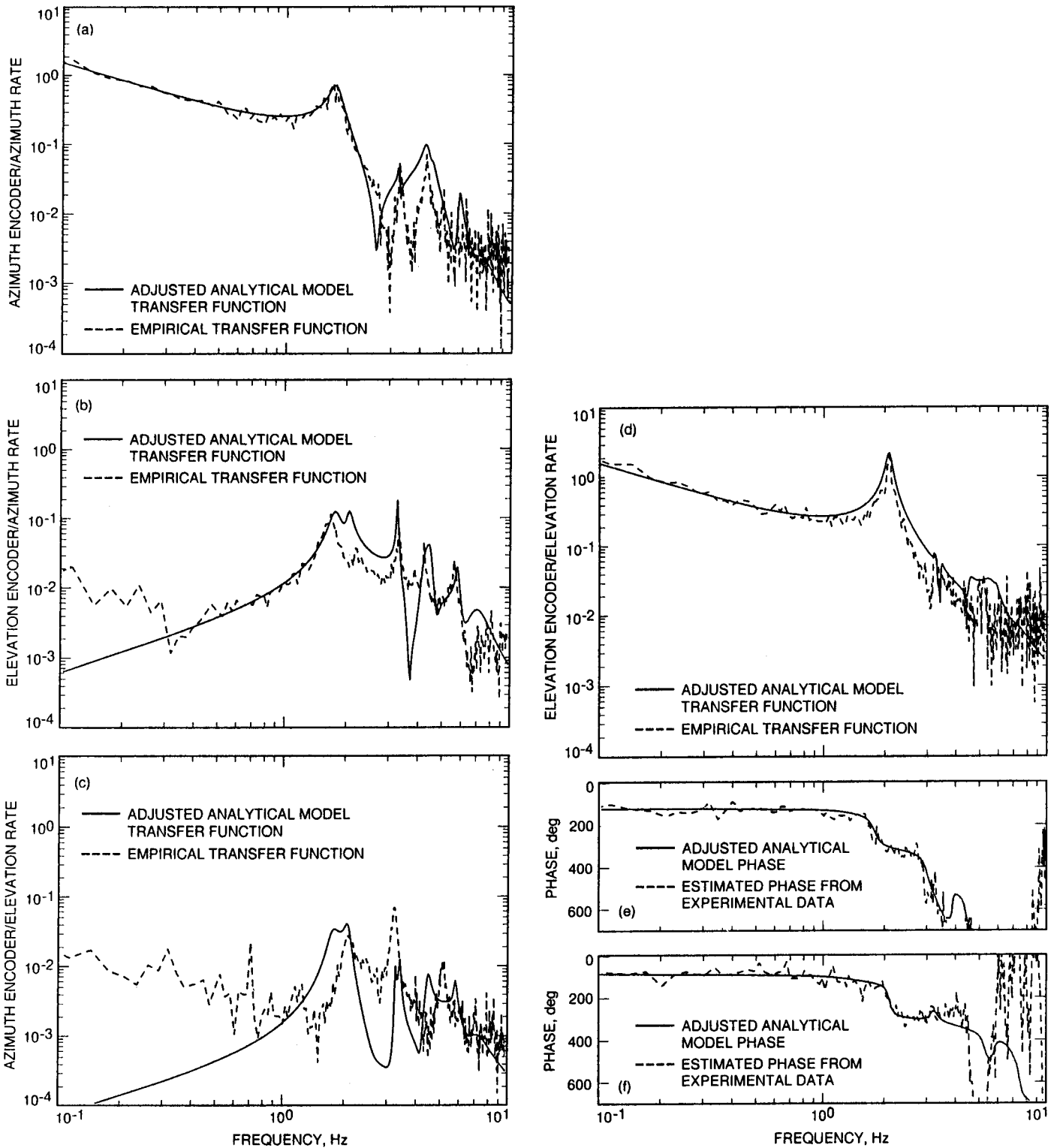
Fig. 2. Magnitude and phase averages: (a) azimuth rate input to azimuth encoder output, (b) azimuth rate input to elevation encoder output, (c) elevation rate input to azimuth encoder output, (d) elevation rate input to elevation encoder output, (e) azimuth rate input to azimuth position output phase, and (f) elevation rate input to elevation position output phase.
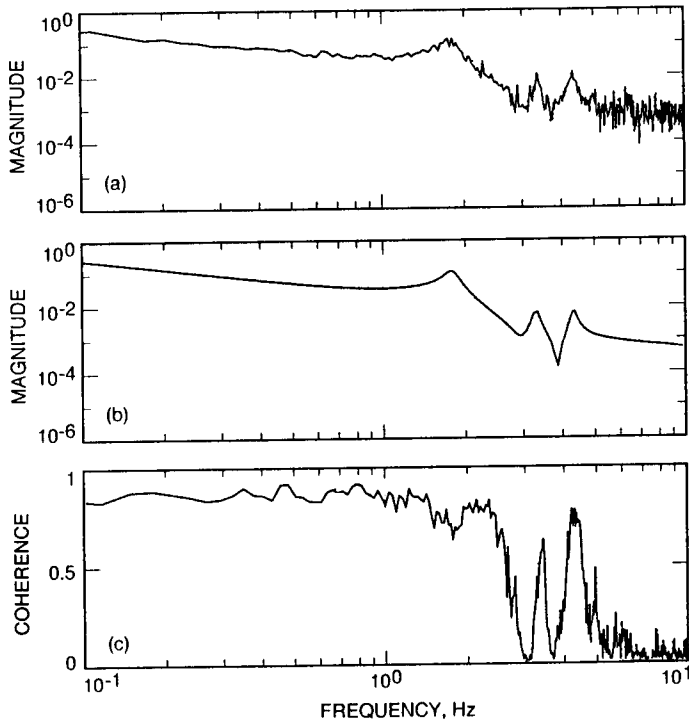
Fig. 3. Azimuth rate Input to azimuth position output: (a) estimated transfer function from SISO data, (b) system identification model transfer function, and (c) coherence of SISO data.
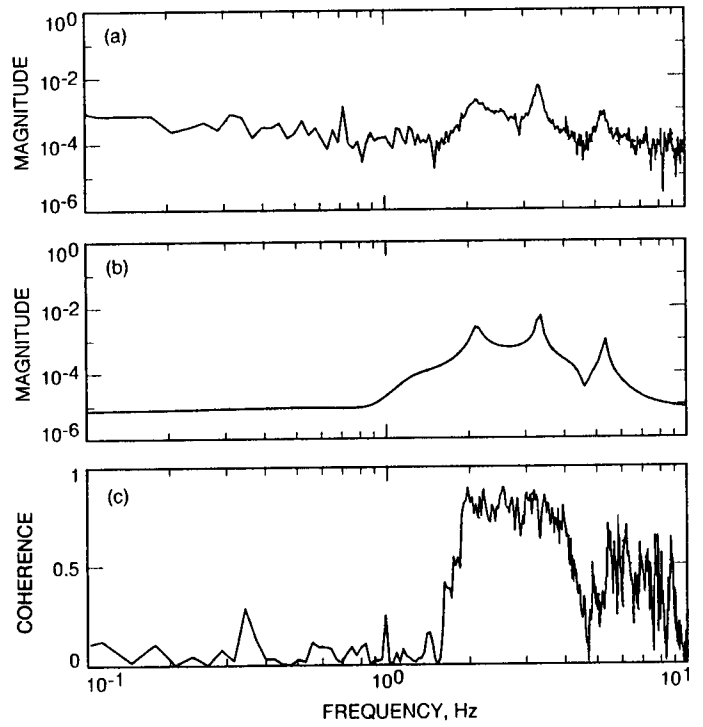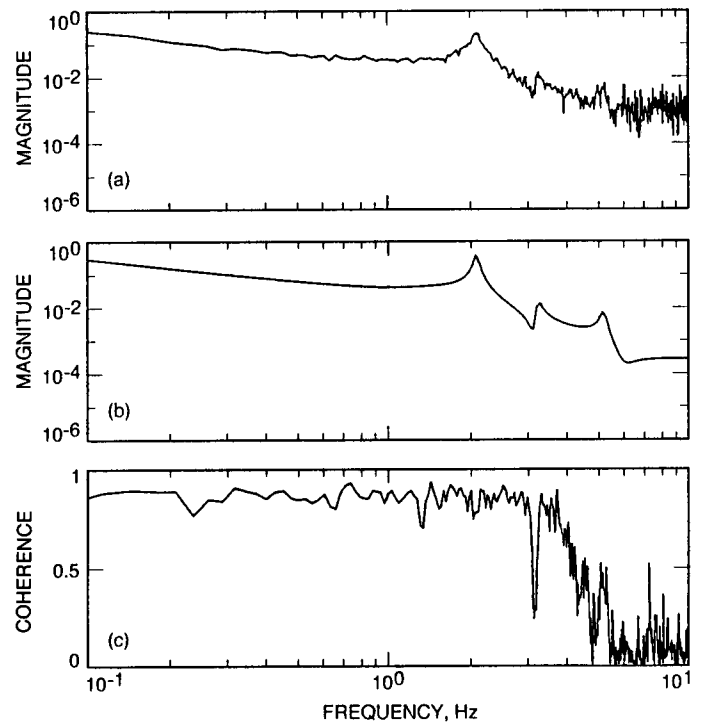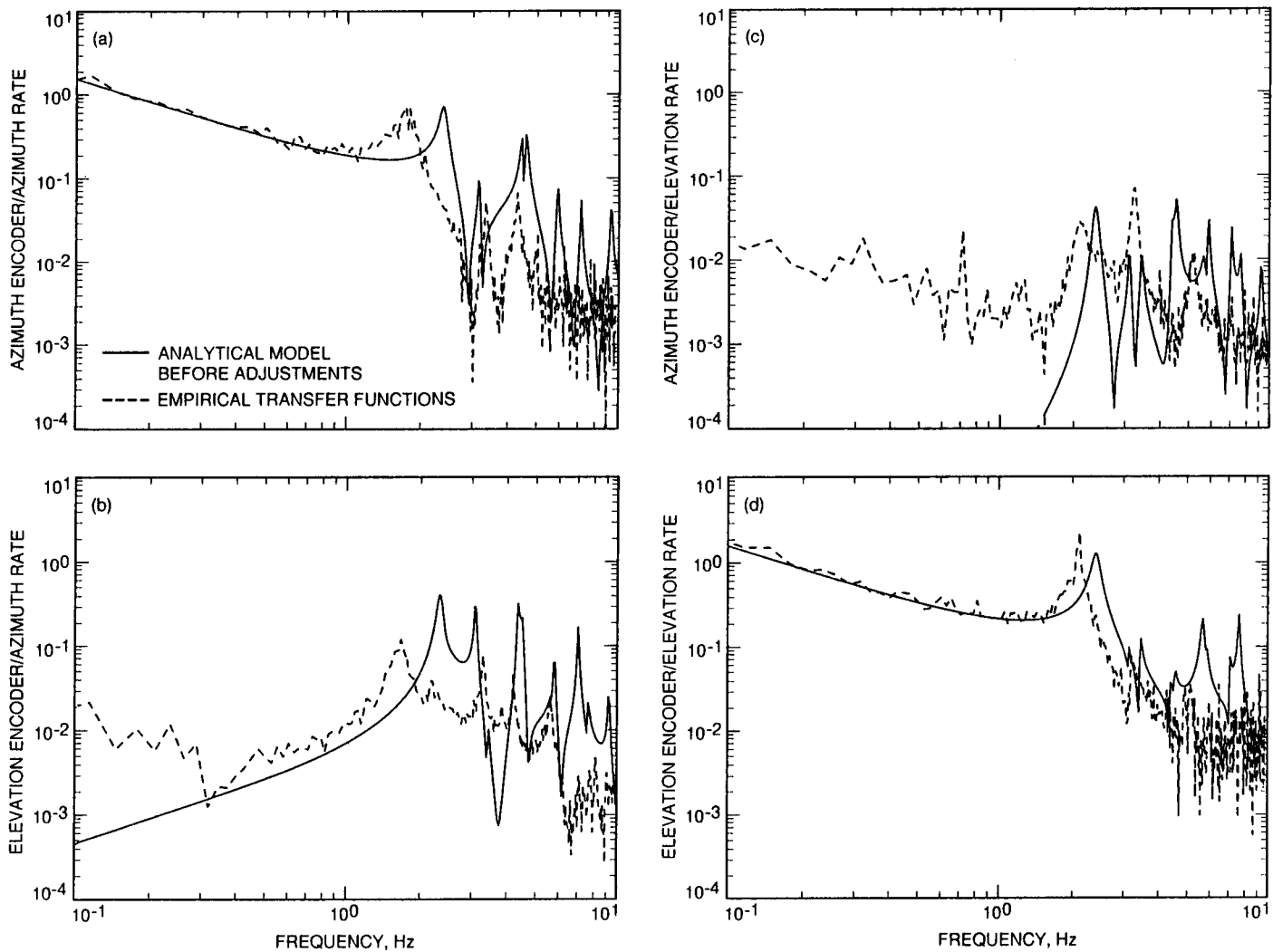
Fig. 5. Elevation rate Input to azimuth position output: (a) estimated transfer function from SISO data, (b) system identification model transfer function, and (c) coherence of SISO data.
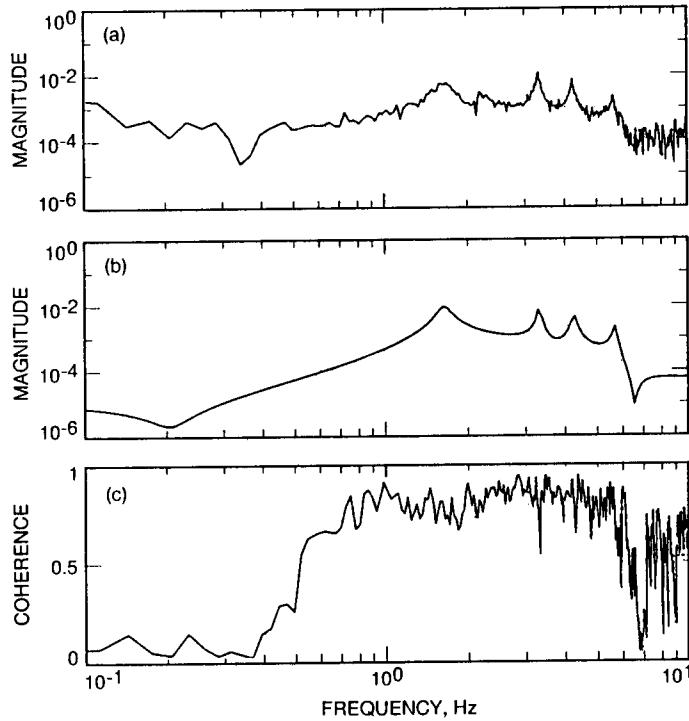
Fig. 4. Azimuth rate Input to elevation position output: (a) estimated transfer function from SISO data, (b) system identification model transfer function, and (c) coherence of SISO data.

Fig. 6. Elevation rate Input to elevation position output: (a) estimated transfer function from SISO data, (b) system identification model transfer function, and (c) coherence of SISO data.

51

Fig. 7. Magnitude plots of the transfer functions from the analytical model and the experimental data: (a) azimuth rate input to azimuth position output, (b) azimuth rate input to elevation position output, (c) elevation rate input to azimuth encoder output, and (d) elevation rate input to elevation encoder output.
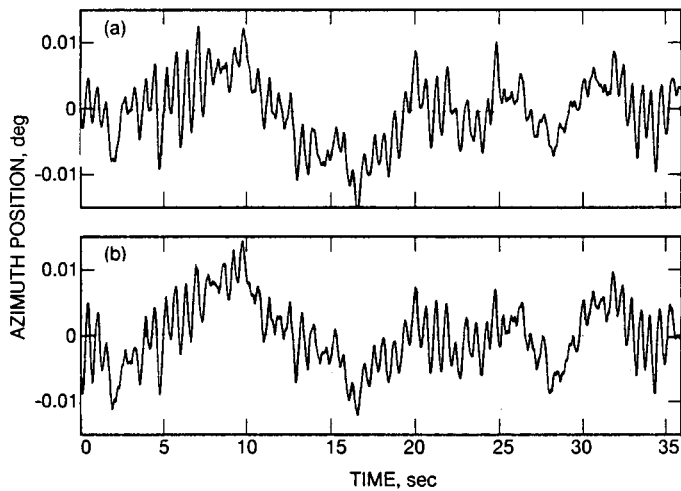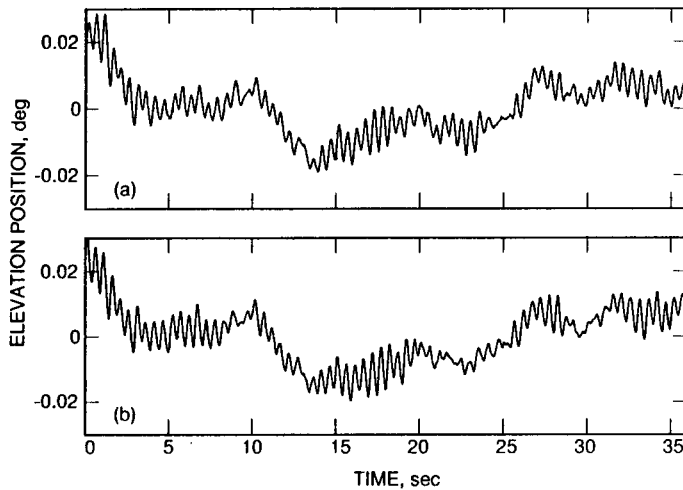
Fig. 8. Detrended azimuth-to-elevation time series output data: (a) measured and (b) simulated.
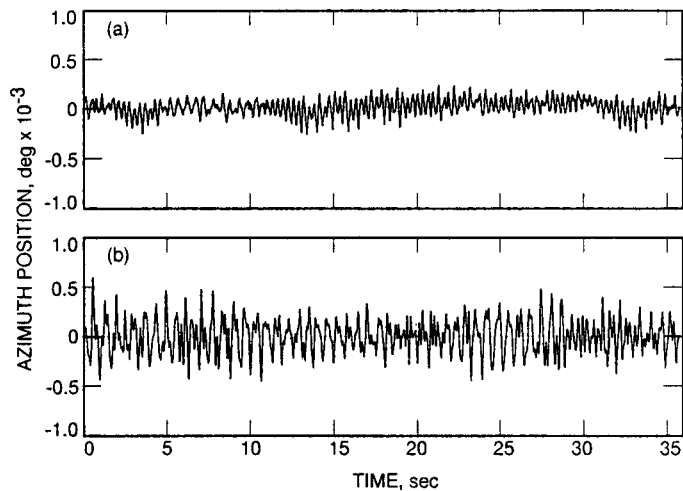
Fig. 10. Detrended elevation-to-azimuth cross-coupling time series output data: (a) measured and (b) simulated.
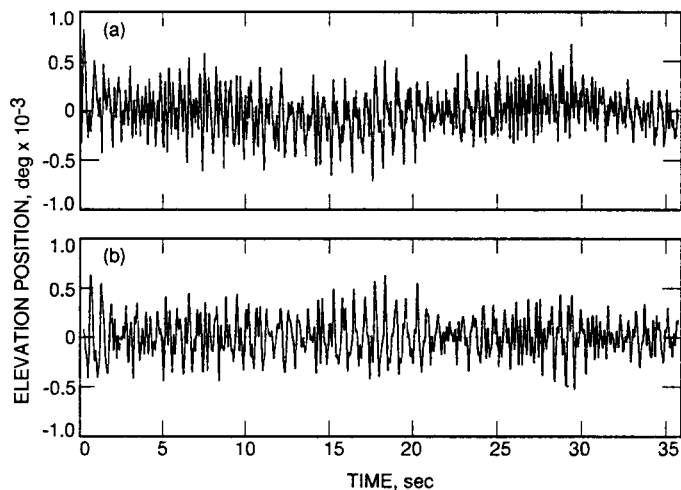
Fig. 9. Detrended azimuth-to-azimuth cross-coupling time series output data: (a) measured and (b) simulated.

Fig. 11. Detrended elevation-to-elevation time series output data: (a) measured and (b) simulated.